Geophysical Research Letters

RESEARCH LETTER
10.1029/2022GL098029

Key Points:

- Relatively simple, dynamic rupture model reproduces near-fault waveforms and source characteristics of the 2016 Kumamoto earthquake
- Large, long-period ground velocities in near-fault regions can be explained by the interaction of propagating rupture and Earth's surface
- Free surface effect on dynamic rupture propagation is enhanced by reflected waves from the boundaries of low-velocity layers

Supporting Information:

Supporting Information may be found in the online version of this article.

Correspondence to:

Y. Kaneko,
kaneko.yoshihiro.4e@kyoto-u.ac.jp

Citation:

Kaneko, Y., & Goto, H. (2022). The origin of large, long-period near-fault ground velocities during surface-breaking strike-slip earthquakes. *Geophysical Research Letters*, *49*, e2022GL098029. https://doi.org/10.1029/2022GL098029

Received 26 JAN 2022
Accepted 5 MAY 2022

Author Contributions:

Conceptualization: Yoshihiro Kaneko, Hiroyuki Goto
Data curation: Yoshihiro Kaneko, Hiroyuki Goto
Formal analysis: Yoshihiro Kaneko, Hiroyuki Goto
Funding acquisition: Yoshihiro Kaneko
Investigation: Yoshihiro Kaneko, Hiroyuki Goto
Methodology: Yoshihiro Kaneko
Project Administration: Yoshihiro Kaneko
Resources: Yoshihiro Kaneko
Software: Yoshihiro Kaneko
Validation: Yoshihiro Kaneko
Visualization: Yoshihiro Kaneko
Writing – original draft: Yoshihiro Kaneko
Writing – review & editing: Yoshihiro Kaneko, Hiroyuki Goto

The Origin of Large, Long-Period Near-Fault Ground Velocities During Surface-Breaking Strike-Slip Earthquakes

Yoshihiro Kaneko[1] and Hiroyuki Goto[2]

[1]Graduate School of Science, Kyoto University, Kyoto, Japan, [2]DPRI, Kyoto University, Kyoto, Japan

Abstract Records of near-fault ground motions from recent surface-breaking earthquakes are characterized by large (> a few m/s), long-period (a few seconds) ground velocity pulses, which may pose significant hazard for tall buildings and large infrastructures. Yet, the generation mechanism is not well understood. Here, using spontaneous rupture simulations, we examine the origin of large velocity pulses observed during the 2016 Mw7.0 Kumamoto (Japan) earthquake. We show that near-fault waveform data as well as seismologically estimated moment and radiated energy can be well reproduced by a relatively simple model with uniform along-strike pre-stress and frictional properties. Our results suggest that large, long-period ground velocities are caused by the dynamic interaction of propagating rupture and the Earth's surface, which is enhanced by reflected waves from the boundaries of low-velocity layers. Such a generic mechanism suggests that large, long-period ground motion is a common occurrence in near-fault regions during surface-breaking, strike-slip earthquakes.

Plain Language Summary Recordings of ground motions during recent large earthquakes show unusually large amplitudes and long duration in the vicinity of the fault rupture. How and why such ground motions were generated remains mystery. We utilize both the numerical simulations of earthquake rupture and ground motion data to investigate the origin of unusually large and long-duration ground motions observed during the 2016 magnitude 7.0 Kumamoto (Japan) earthquake. We find that the observed ground motions can be well explained by a model that accounts for the interaction of propagating earthquake rupture with the Earth's surface. We provide an explanation for why unusually large and long-duration ground motions are expected in the regions close to the fault ruptured during any surface-breaking, strike-slip earthquake. Our study highlights the important role of rupture dynamics in estimating seismic hazard for tall buildings and large infrastructures (e.g., dams and bridges) in major cities around the world.

1. Introduction

Ground motions with unusually large (a few m/s) velocity pulses have been observed during large destructive earthquakes, such as the 1999 Mw7.6 Chichi (Taiwan), 1999 Mw7.6 Izmit (Turkey), 2002 Mw7.9 Denali (Alaska), and 2016 Mw7.0 Kumamoto (Japan) (e.g., Barka, 1999; Dunham & Archuleta, 2004; Ji et al., 2003; Kobayashi et al., 2017). During the 1999 Chichi earthquake, seismic stations close to the Chelungpu fault recorded up to 3 m/s of surface ground velocity, which may have been induced by well-known hanging wall effects (Abrahamson & Somerville, 1996; Ji et al., 2003). For strike-slip events, the 1999 Izmit and 2002 Denali earthquake produced large velocity pulses recorded approximately 3 km away from the faults ruptured during these events, which were attributed to the Mach waves formed by the propagation of supershear ruptures (e.g., Dunham & Archuleta, 2004; Bernard & Baumont, 2005). Large velocity pulses, often confined within a few kilometers from the fault trace, pose significant hazard for buildings and infrastructures and are of prime concern for seismologists and earthquake engineers (e.g., Morii et al., 2020). Yet, the mechanism responsible for the generation of large ground-velocity pulses and how common they are, especially for subshear, strike-slip earthquakes, is not well understood.

The 2016 Mw7.0 Kumamoto earthquake ruptured the Hinagu and Futagawa faults (Asano & Iwata, 2016; Hao et al., 2017; Kubo et al., 2016; Yue et al., 2017) and was captured by several near-fault seismic stations, one of which recorded a large (>2.5 m/s), fault-parallel velocity pulse characterized by 2–3 s dominant period (Figure 1; Table S1 in Supporting Information S1). The seismic station is located in the Nishihara village, central Kyushu (Japan), which is 650 m away from the surface fault trace (Figure 1a). The pulse-like nature of this velocity record indicates that the earthquake rupture propagated as a slip pulse, characterized by an annular zone propagating

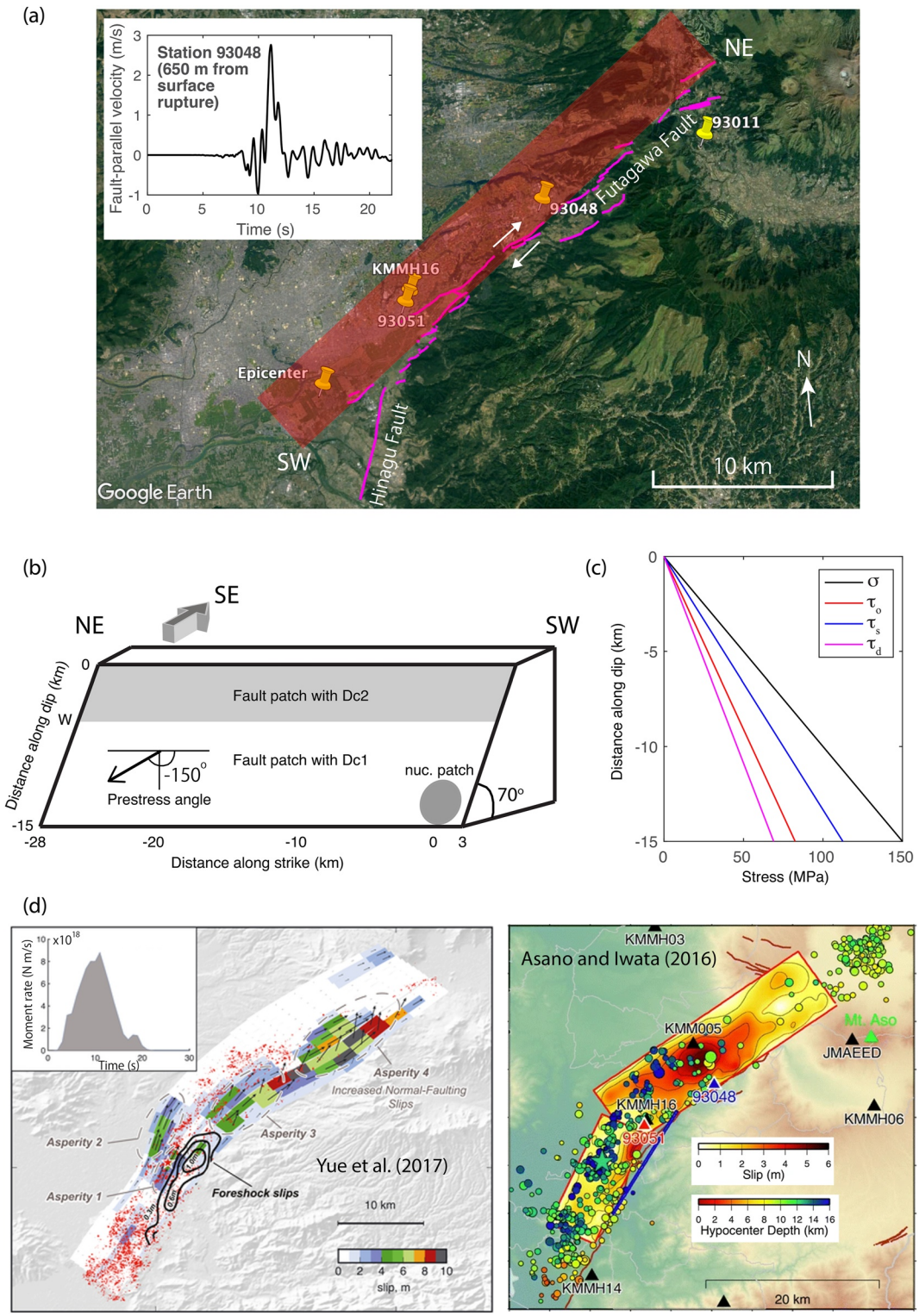
(a)
Station 93048 (650 m from surface rupture)
Fault-parallel velocity (m/s)
Time (s)
NE
93011
Futagawa Fault
93048
KMMH16
93051
Epicenter
Hinagu Fault
SW
N
10 km
Google Earth
(b)
SE
NE
SW
Distance along dip (km)
W
Fault patch with Dc2
Fault patch with Dc1
-150°
Prestress angle
nuc. patch
70°
Distance along strike (km)
(c)
σ
τo
τs
τd
Distance along dip (km)
Stress (MPa)
(d)
Moment rate (N m/s)
Time (s)
Asperity 4
Increased Normal-Faulting Slips
Asperity 3
Asperity 2
Asperity 1
Foreshock slips
Yue et al. (2017)
10 km
slip, m
KMMH03
Asano and Iwata (2016)
KMM005
Mt. Aso
JMAEED
KMMH16
93048
KMMH06
93051
Slip (m)
Hypocenter Depth (km)
KMMH14
20 km

Figure 1.

outward from the hypocenter (Heaton, 1990). However, linking the ground motion record to the evolution of on-fault coseismic slip is not straightforward as the station is not located exactly on the fault.

The generation mechanism of the large velocity pulse is unknown. Kobayashi et al. (2017) used joint inversion of strong motion, teleseismic and geodetic data to develop a kinematic model of the Kumamoto earthquake and concluded that the largest velocity pulse at Station 93048 may have been caused by coherent wave arrivals resulting from simultaneous slip of subparallel faults in the vicinity of the station. If their interpretation is correct, the occurrence of large velocity pulses may require special circumstance (e.g., superposition of seismic waves from multiple fault ruptures) and hence would be relatively uncommon. In another study, Urata et al. (2017) conducted dynamic rupture simulations to reproduce the overall source characteristics of the Kumamoto earthquake, but did not focus on replicating the velocity pulses. Recently, Irikura et al. (2019) introduced shallow (approximately 3 km) fault patches of long-period-motion generation that are unconventional to standard kinematic ground motion approaches (e.g., Irikura & Miyake, 2011) and reproduced the velocity pulses observed at Station 93048. However, the physical origin of long-period-motion generation fault patches proposed by Irikura et al. (2019) as well as how common such features are during large earthquakes remain unclear.

To understand the origin of the large velocity pulses observed during the Kumamoto earthquake, we construct relatively simple, dynamic rupture models and attempt to reproduce observed waveforms at a set of near-fault stations. Dynamic rupture simulations have been used to understand the characteristics of near-fault waveforms (e.g., Dunham & Archuleta, 2005), to infer friction properties of ruptured faults (e.g., Weng & Yang, 2018), and to numerically study the characteristics of near-fault ground motions (e.g., Dalguer et al., 2008; Hu et al., 2019; Pitarka et al., 2009). In particular, unlike kinematic source models, the interaction of free surface and fault rupture is physically accounted for in dynamic rupture models (e.g., Day et al., 2005; Kaneko & Lapusta, 2010). We compare a set of source models with observations, and discuss the implications for earthquake physics and ground motion hazard.

2. Model Setup

We consider a northeast striking, northwest dipping Futagawa fault embedded into an elastic, layered half-space (Figure 1b). The assumed 1-D velocity model derived from a regional 3D velocity model (Koketsu et al., 2012) is shown in Table S2 in Supporting Information S1. Since previous slip inversion results indicate relatively minor contributions of the Hinagu fault during the mainshock (Figure 1d), we consider the Futagawa fault only. We assume that the Futagawa fault that ruptured during the mainshock is a 31.0 by 15.0 km planar segment, with its surface trace determined by fitting a straight line to the southern and northern ends of the Fatagawa fault surface traces identified in field studies (Shirahama et al., 2016) (Figure 1a). The dip of the fault is assumed to be 70°, consistent with the Japan Meteorological Agency's (JMA) focal mechanism. The center of the fault plane is located at latitude 32.834, longitude 130.868, and the depth of 7.05 km (Figure 1a).

We aim to analyze a set of relatively simple models. As such, the initial stresses and friction properties are assumed to be uniform along the fault strike and only vary with depth (Figure 1c). The constitutive response of the fault is governed by a linear slip-weakening friction law (Ida, 1972; Palmer & Rice, 1973), in which the friction coefficient linearly decreases from its static value μ_s to a dynamic value μ_d over a characteristic slip distance D_c. Since D_c which is proportional to the fracture energy may be related to the width of a fault damage zone and decrease with depth (e.g., Ide & Takeo, 1997), we assume that the shallower portion of the fault is characterized by a larger value, D_{c2}, than the deeper one, D_{c1} (Figure 1b; Table S3 in Supporting Information S1). Effective normal stress σ linearly increases with depth via $\sigma = 10.0 \times z$ (MPa), where z is down-dip distance in km. As a result, both the static (τ_s) and dynamic (τ_d) strength as well as the magnitude of initial shear stresses τ_0 linearly vary with depth (Figure 1c). To reproduce the right-lateral and normal faulting, we approximate the direction of shear stresses using the JMA focal mechanism and set the initial shear stress direction with a rake of −150° in

Figure 1. (a) Map of a Kumamoto earthquake source region. Purple lines indicate the surface traces of faults ruptured during the Kumamoto earthquake sequence (Shirahama et al., 2016). Yellow pins correspond to either the epicenter, KiK-net or JMA strong motion stations, with the corresponding peak ground accelerations and velocities listed in Table S1 in Supporting Information S1. The inset shows the fault-parallel component of unfiltered velocity recorded at station 83048 in the Nishihara village. A red rectangle shows a 31 km by 15 km, 70° dipping planar fault assumed in this study. (b) A sketch showing the fault geometry of dynamic rupture model. Gray circle shows a nucleation patch where the rupture is forced to initiate. The shallow fault patch with the depth extent W is characterized by a larger value of slip-weakening distance D_{c2} than the deeper counterpart D_{c1}. (c) Depth dependence of effective normal stress σ, initial shear stress τ_0, peak strength τ^p, and dynamic strength τ^d assumed in this study. (d) Kinematic source models of the Kumamoto earthquake from Yue et al. (2017) and Asano and Iwata (2016).

the fault plane (Figure 1b). Slip velocity vector is assumed to be always parallel to the shear traction vector at each instant in time at all fault node points, as commonly done in dynamic rupture simulations (e.g., Bizzarri & Cocco, 2005; Kearse & Kaneko, 2020).

The fault is initially at rest, and dynamic rupture is initiated by imposing a smooth, time-dependent growth of the rupture front within a circular nucleation patch located at 12.2 km depth (or 13.0 km down-dip distance) (a gray circle in Figure 1b), consistent with the JMA hypocentral depth of 12 km. Once the rupture nucleates, it spontaneously propagates outside the nucleation patch. The numerical code we use is based upon a spectral element method (Ampuero, 2002; Kaneko et al., 2008), which has been verified through a series of benchmark exercises (Harris et al., 2018). The details of the friction law implementation, nucleation procedure, and numerical resolution are described in Supporting Information S1.

3. Result

3.1. Comparison of Simulations With Observations

We first vary parameter μ_d and hence dynamic stress drop on the fault (Table S3 in Supporting Information S1), and find a set of rupture scenarios with $\mu_d = 0.47$ that lead to the moment magnitude of approximately 7.0 and slip distribution comparable to those in InSAR-derived slip models (Fukahata & Hashimoto, 2016; Yue et al., 2017). We then vary on-fault parameters D_{c2} and its depth extent W (Figure 1b) to come up with our preferred model that best fits a set of observations. Note that while the boundary between D_{c1} and D_{c2} might represent a significant change in the width of the damaged fault zone at depths (e.g., Cochran et al., 2009), we introduce this parameterization for simplicity and convenience, to control the rupture arrival times, which mainly affect the timing of dominant phases in strong-motion waveforms as discussed later.

We quantify the waveform misfit and compare near-fault waveforms between a set of forward simulations and observations (Figure 2). We define net normalized misfit χ, following Goto et al. (2019), as

$$\chi = \sum_{i}^{N} \sum_{j}^{3} \frac{|\mathbf{d} - \mathbf{m}|^2}{|\mathbf{d}||\mathbf{m}|}, \tag{1}$$

where $\mathbf{d}$ and $\mathbf{m}$ are observed and computed seismograms, respectively, $|\mathbf{d} - \mathbf{m}|$ is the root-mean-square of the residuals, and the summation is taken over three components and the number of stations N ($N = 4$ in this case). Both the observed and computed waveforms are low-pass-filtered at 2 s, to avoid prominent site effects that are observed at several stations (Figure S1 in Supporting Information S1). The high-frequency (>0.5 Hz) site effects were also reported from an aftershock study in this region (Yamanaka et al., 2016).

The resulting waveform misfits as a function of D_{c2} and its depth extent W are shown in Figure 2a. As the value of D_{c2} or W increases, the overall rupture speed decreases due to larger fracture energy (i.e., larger energy dissipation at the crack tip) and the corresponding waveform misfit increases (Figure 2a). In the cases with smaller D_{c2} or W, the overall rupture speed increases and the waveform misfit gets larger. Hence the arrival times of domain phases are sensitive to the fracture energy distribution, consistent with the results of dynamic inversion studies (e.g., Goto & Sawada, 2010). The tradeoff between the value of D_{c2} and its depth extent W (Figure 2a) suggests that the on-fault distribution of D_c is difficult to constrain from the low-frequency (<0.5 Hz) waveform data alone. This is also evident from the fact that a model with uniform $D_c = 0.15$ m over the fault and different nucleation parameters can reproduce a set of observed waveforms reasonably well (Figure S3 in Supporting Information S1).

We find that comparing radiated energy computed from dynamic rupture simulations and that estimated from teleseismic waveforms can provide further constraints on the model parameters. We calculate radiated energy E_r in dynamic rupture simulations via (e.g., Kaneko & Shearer, 2014; Ma & Archuleta, 2006)

$$E_r = \int_{\Sigma} \frac{\tau_o(\xi) + \tau_f(\xi)}{2} D(\xi) d\Sigma - \int_0^{\infty} \int_{\Sigma} \tau(\xi, t) V(\xi, t) d\Sigma dt, \tag{2}$$

where τ_o and τ_f are the magnitude of the initial and final shear stresses, respectively, D is the magnitude of the final slip, $\tau(\xi, t)$ is the magnitude of shear stresses, $V(\xi, t)$ is the magnitude of slip rates, and Σ is the rupture area. Our preferred model indicated by a black circle in Figure 2a results in $E_r = 2.7 \times 10^{15}$J, which is 50% larger

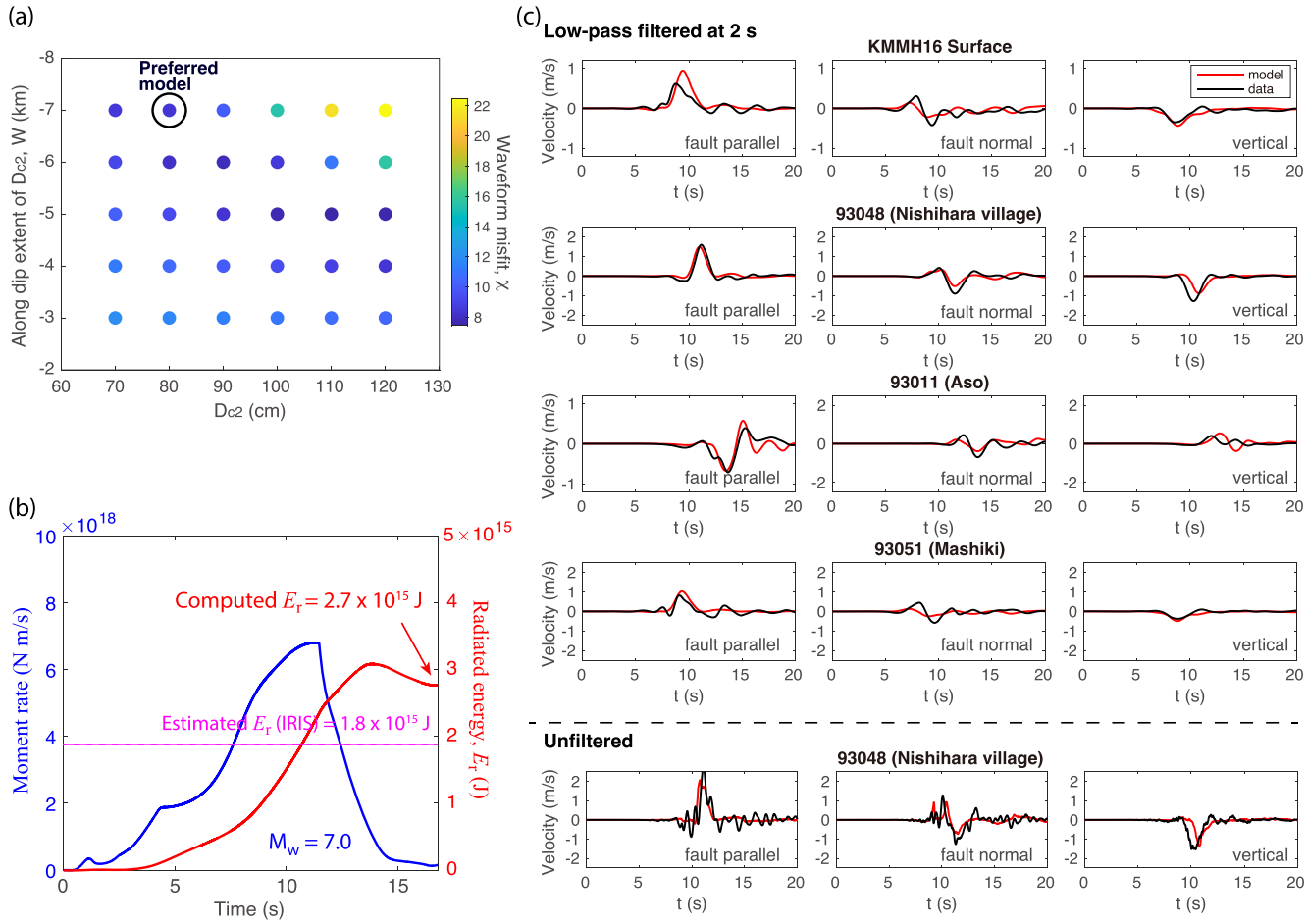

Figure 2. Comparisons between simulated and observed waveforms and source characteristics. (a) Dependence of waveform misfit on the value of D_{c2} and the along-dip extent W, as defined in Figure 1. In all these cases, $\mu_d = 0.47$ is assumed. Misfit is defined in the main text. For the calculation of misfit, both the data and synthetic waveforms are low-pass-filtered below 2 s. There is a trade-off between D_{c2} and the along-dip extent W. (b) Moment rate function (blue) and radiated energy (red) in the preferred model. Radiated energy estimated from teleseismic records (dashed purple line) is also indicated. (c) Waveform fits at 4 near-fault stations in the preferred model. Time $t = 0$ corresponds to the JMA origin time of the event. The total waveform misfit in the preferred model is $\chi = 8.4$. For Station 93048, both the filtered and unfiltered waveforms are shown. The locations of these stations are indicated in Figure 1. The model reproduces the observed waveforms well.

than that inferred from observations (IRIS DMC, 2013, https://ds.iris.edu/spud/eqenergy/11545444) (Figure 2b). However, given that the observed E_r is estimated from the teleseismic records (Convers & Newman, 2011), which would be deficient in high-frequency energy from the source due to frequency-dependent anelastic attenuation (e.g., Yoshimoto et al., 1993), and that a factor of approximately 2 uncertainty generally presents in previous estimates of radiated energy (e.g., Venkataraman & Kanamori, 2004; Ye et al., 2016), the agreement between the computed and observed E_r is reasonable. Larger D_{c2} or a smaller W leads to an overestimation of radiated energy by a factor of 2 and greater while the seismic moment is relatively insensitive to these parameters (Figure S2 in Supporting Information S1). Based on the waveform misfits (Figure 2a) and radiated energy misfits (Figure S2 in Supporting Information S1), we select a preferred model indicated by the black circle in Figure 2a with the corresponding moment rate function (Figure 2b), which is in agreement with that derived from kinematic slip inversion (Figure 1d).

Remarkably, at Station 93048 where the largest fault-parallel velocity pulse is observed, the synthetic seismograms in the preferred model fit the data well (Figure 2c). The onset, amplitude and polarities of dominant phases for three components are well matched. Even when the unfiltered record is used, the agreement remains fairly well (Figure 2c), while high frequencies (>0.5 Hz) at the other stations are contaminated by site effects (Figure S1 in Supporting Information S1) that are not included in the present model. The evolution of the rupture and final slip distribution (Figure 3) is qualitatively consistent with those on the Futagawa fault in kinematic models

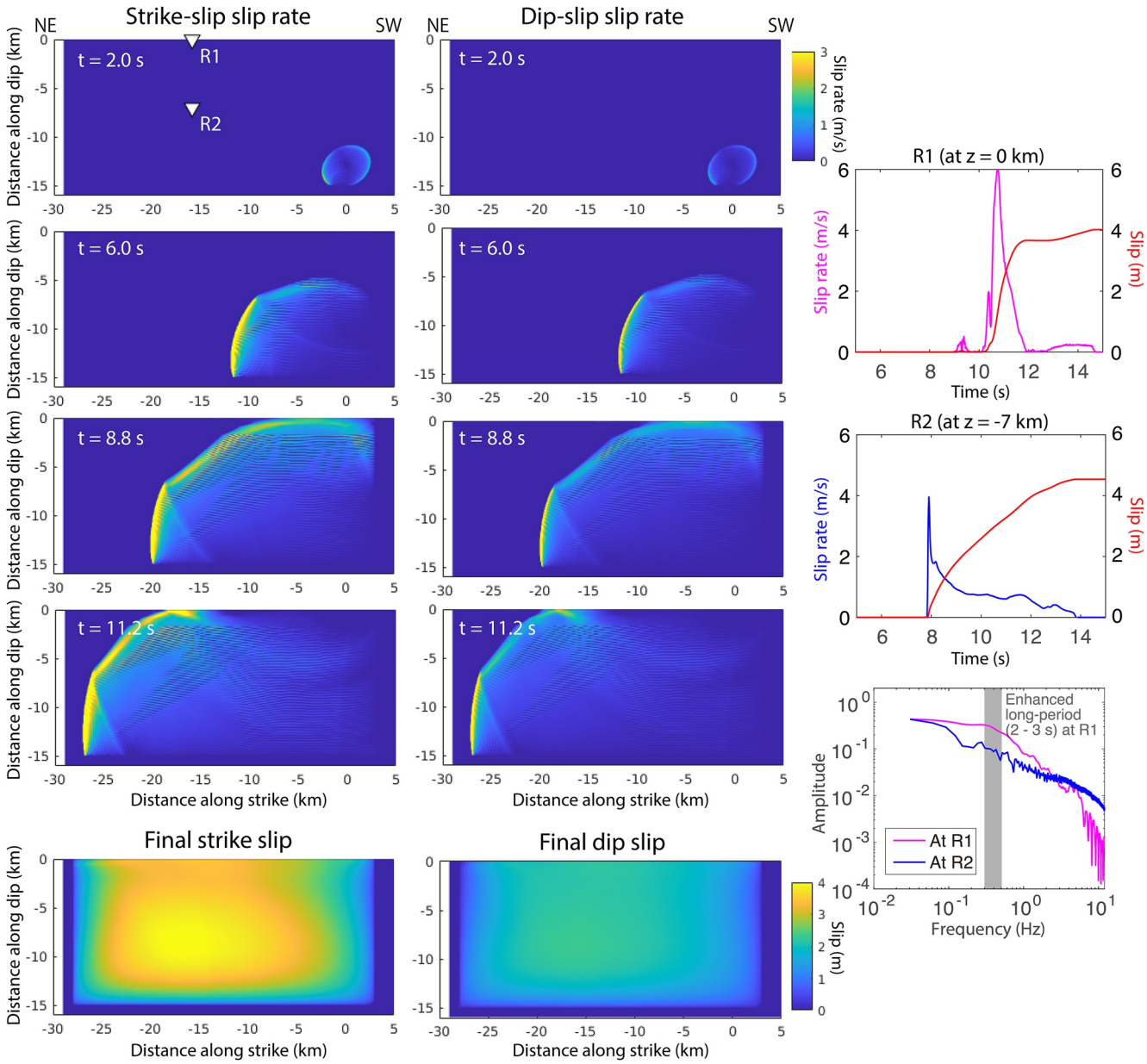

Figure 3. Snapshots of slip rates and final slip distributions in the preferred model. White triangles show on-fault receivers R1 and R2. Receiver R1 is located on the fault trace closest to Station 93048, and receiver R2 is located at 6.5 km depth (i.e., −7.0 km along-dip distance). When the rupture front encounters the region of D_{c2}, the rupture slows down due to increased fracture energy. The rupture speed further decreases at shallow depths (in the top 1.6 km) due to the low-velocity layers. When the rupture front reaches the free surface, a reflected rupture front emerges and constructively interferes with the main rupture front. Slip rates at shallow depths are further enhanced by reflected waves from the boundaries of the low-velocity layers. Stripes in some snapshots are high-frequency numerical artifacts, which do not affect the main outcome of the model. Inset panels show slip and slip-rate evolution at R1 and R2 and the spectra of the slip rate functions at R1 and R2 (purple and blue curves). The amplitude of long-period slip rates at R1 is larger than that at R2.

(Figure 1d). At approximately 8 s after the origin time, the rupture reaches the Earth's surface and propagates predominately toward the northwest at subshear speeds (Figure 3). The rupture eventually arrests in the vicinity of the Aso volcano, and the final slip distribution is broadly consistent with that derived from an InSAR-derived slip model (Fukahata & Hashimoto, 2016). The average static stress drop in the preferred model is 5.8 MPa, which is within a typical range of shallow crustal earthquakes (i.e., 1–10 MPa) (Kanamori & Anderson, 1975).

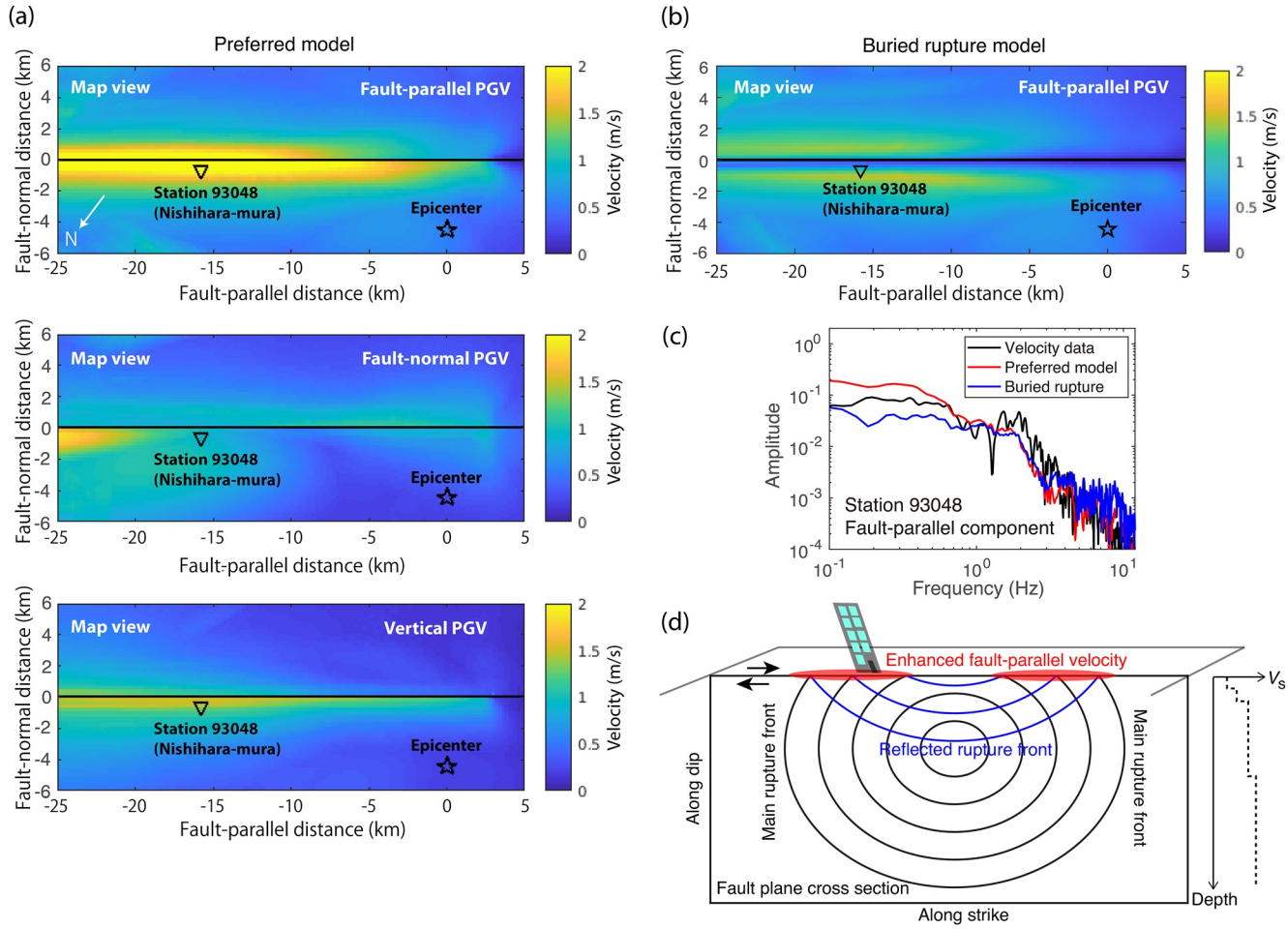

Figure 4. (a) Distribution of peak ground velocities (PGVs) on the Earth's surface in the preferred model. PGVs in individual components (fault-parallel, fault-normal and vertical) are shown. Regions of large (>1.5 m/s) fault-parallel PGVs are confined within the regions ±1 km from the fault trace. PGV distributions across the fault are asymmetric because the fault dips to the northwest. (b) Distribution of fault-parallel PGVs for the case with buried rupture as shown in Figure S4 in Supporting Information S1. (c) Computed and observed spectra of fault-parallel ground velocities at Station 93048. (d) Cartoon illustrating the mechanism of enhanced fault-parallel PGVs due to a free surface effect. Reflected rupture front constructively interferes with the main rupture front, resulting in larger, fault-parallel ground velocities in the vicinity of the fault. The rupture process is enhanced by reflected waves from the boundaries of shallow low-velocity layers.

3.2. The Origin of Large, Long-Period Ground Velocities at Station 93048

Given the overall agreement between the preferred model and observations, we examine the physical origin of the largest velocity pulse observed at Station 93048. As expected, the ground velocity pulse is associated with pulse-like rupture sweeping through a section of the fault close to Station 93048 (Figure 3). The spatial width of the propagating slip pulse in the shallow section of the fault is 5–6 km near Station 93048 (Figure 3). In this case, the pulse-like rupture forms due to stopping phases generated by the slip arrest predominately at the south-western fault edge (corresponding to the presence of unbroken barrier there). Compared to shallow depths, slip duration at greater depths is longer (compare Receivers R1 and R2 in Figure 3). However, amplitude spectra of the slip-rate functions show that the long-period (2–3 s) is enhanced at shallow depths (Receiver R1) (Figure 3). Hence, this suggests that the long-period nature of the large ground-velocity pulse is linked to the free surface effect, not to the stopping phase. Note that the enhanced long period of the slip-rate function at shallow depths is not caused by D_{c2}, as the result with uniform D_c over the fault also shows such characteristics (Figure S3 in Supporting Information S1).

To understand the cause of the particularly large velocity amplitude at Station 93048, we plot the peak-ground velocity (PGV) at the Earth's surface (Figure 4a). Large PGVs are in the fault-parallel component and are confined within regions ±1 km from the fault and several kilometers away from the region directly up-dip of

the hypocenter (Figure 4a), which may explain why Station 93048 recorded the largest ground-velocity amplitude, compared to the other stations (Figure 2c). The large, near-fault fault-parallel velocities are caused by the dynamic interaction of the propagating, subshear rupture and that reflected by the free surface (Figure 3). As the main rupture front encounters the free surface, a reflected rupture front emerges and propagates with and slightly behind the main rupture front (Figure 3), enhancing the ground velocity amplitude and duration in the vicinity of the fault trace (Figure 4a).

To further examine the free surface effect, we consider three additional models: (a) a model with buried rupture where the shallowest portion of the fault (in the top 0.8 km) is assumed to be an unbreakable barrier, (b) a model with a homogeneous half-space, and (c) a model with a homogeneous half-space with uniform D_c. The buried-rupture model (Model a) does not show large, long-period fault-parallel ground velocities at Station 93048 while the waveform fits at the other stations are still satisfactory (Figures 4b and S4 in Supporting Information S1). Comparison of computed and observed ground velocity spectra at Station 93048 shows that the amplification of long-period ground velocities is present in both the data and preferred model, but not in the buried-rupture model (Figure 4c), indicating the importance of the free surface effect.

The free surface effect on amplified ground velocities localizes, and the long-period slip rates at shallow depths diminish in the models with a homogeneous half-space with nonuniform and uniform D_c (Models b and c) (Figures S5 and S6 in Supporting Information S1), suggesting that the shallow, low-velocity layers in the preferred model also contributes significantly to the long-period ground-velocity amplification. We note that the free surface effect is not completely isolated even in the (unrealistic) homogeneous half-space models since the effective normal stress is depth-dependent, resulting in smaller slip rates at shallower depths and suppressing the free surface effect. As the resonance period of the top low-velocity layer, approximated as $4H/V_s = 2.3$ s where H is the thickness (Singh et al., 1988), coincides with the dominant period of the ground-velocity pulse, one may suspect that the path effect influences the observed ground velocity amplification. However, the lack of long-period ground-velocity amplification at Station 93048 in the buried-rupture model with the same layered velocity structure (Figure 4c) suggests that the path effect does not significantly contribute to the near-fault ground velocities. Instead, reflected waves from the boundaries of shallow low-velocity layers enhances the rupture process (i.e., the source effect) (Figure 3), amplifying the free surface effect.

4. Discussion

Our results suggest that the large, long-period (2–3 s) ground velocities in the near-fault regions are associated with the amplified, long-period slip rates at shallow depths due to the free surface effect, which is enhanced by the low-velocity layers. To ensure that this mechanism is not just specific to the Kumamoto earthquake, we confirm the occurrence of large, fault-parallel PGVs in the near-fault region in a model with pure strike-slip pre-stress (with a pre-stress rake angle of 180°) (Figure S7 in Supporting Information S1). We note that the 1D velocity profile we assume is quite general, and V_s in the shallowest layer corresponds to "hard rock" site conditions (Boore & Joyner, 1997). In order to assess the influence of assumed velocity structure, we additionally consider a model with a deeper extent of the shallowest low-velocity layer, which shows an increased dominant period of slip rates at shallow depths, resulting in larger, long-period ground velocities at Station 93048 (Figure S8 in Supporting Information S1). Furthermore, since prestress within shallow low-velocity layers may be smaller than that of high-velocity media (Kaneko et al., 2011; Rybicki, 1992), we consider a model with the initial shear stresses that are proportional to the shear modulus (Harris et al., 2018) and confirm that the result of this model is qualitatively similar to that of the preferred model (Figure S9 in Supporting Information S1).

Our results suggest that event-specific conditions, such as long-period generation fault patches (Irikura et al., 2019) or the simultaneous slip of subparallel faults (Kobayashi et al., 2017), are not required to generate the large, velocity pulses observed at near-fault stations. Our results imply that the physical origin of long-period-motion generation fault patches proposed by Irikura et al. (2019) may simply reflect the dynamic interaction of propagating rupture and the Earth's surface combined with the enhanced rupture process on a fault bisecting shallow low-velocity layers. Our proposed mechanism is quite general, suggesting that a large, fault-parallel velocity in near-fault regions could occur during any surface-breaking, strike-slip earthquake (Figure 4d), which could pose significant hazard for tall buildings and large infrastructures (e.g., dams and bridges) in major cities around the world.

Free surface effects in dynamic rupture propagation and near-fault ground motions have been studied theoretically (e.g., Dalguer et al., 2008; Hu et al., 2019; Kaneko & Lapusta, 2010; Pitarka et al., 2009; Wada & Goto, 2012). Our results are consistent with the previous numerical results in that a free surface can amplify the near-fault ground motions. A recent study on dynamic rupture modeling of coseismic slickenlines (Macklin et al., 2021) demonstrates the importance of a shallow low-velocity medium on the resulting rupture characteristics. Our study, for the first time, provides strong observational evidence of long-period ground motion amplification due to the free surface effect enhanced by shallow low-velocity layers.

In our preferred model, W (i.e., the depth extent of D_{c2}) is 7 km, which might indicate a significant change in the width of the damaged fault zone at depths. However, if a damaged fault zone is responsible for the distribution of D_c, continuously varying D_c along dip may be more consistent with inferred damaged fault zones at depths (e.g., Cochran et al., 2009). Hence, we further consider models with linearly decreasing D_c with depth (Figure S10 in Supporting Information S1). We find that the waveform misfit in the best-fitting case is indeed comparable to that of our preferred model (Figure S10 in Supporting Information S1), supporting our interpretation that the distribution of D_c may be related to the width of the damaged zone at depths.

Accurately estimating the spatial distribution of slip-weakening distance D_c on faults remains challenging, even with several near-fault stations. To constrain D_c on the fault using an independent technique, we follow the method of Mikumo et al. (2003) and measure the amount of unfiltered fault-parallel displacement at the time of the peak ground velocity at Station 93048, which is multiplied by the factor of 2 to obtain a proxy for D_c on the fault, referred to as D_c'' (Figure S11 in Supporting Information S1). The estimated D_c'' is 0.9 m at Station 93048 (Figure S11 in Supporting Information S1), in close agreement with $D_{c2} = 0.8$ m inferred from the preferred model (Figure 2a). In addition, applying the same technique to the synthetic waveforms in both the preferred model and the model with uniform value of $D_c = 0.15$ m, we find that D_c'' obtained from the near-fault waveforms agree fairly well with the assumed D_c on the fault (Figure S12 in Supporting Information S1). Hence, this technique may provide additional constraints on the parameters of the dynamic model. At the same time, this technique is capable of resolving D_c only in the localized, shallow (upper approximately 2–3 km) part of the fault (Figure S12 in Supporting Information S1) (Kaneko et al., 2017), and hence, constraining the spatial distribution of slip-weakening distance D_c over the fault remains difficult and would require multiple receivers in the close vicinity (<1 km) of the fault.

Our results indicate that the duration of the propagating slip pulse in the shallow section of the fault is quite long (2–3 s), with the corresponding spatial width of 5–6 km, and is controlled by both the stopping phases originating from the fault edge and the free surface effect in this case. Studies analyzing near-fault waveform data and finite-fault source inversion (Heaton, 1990; Melgar & Hayes, 2017; Somerville et al., 1999) suggested that pulse-like ground velocities are generated by propagating slip pulses during large earthquakes. Several ideas have been proposed to explain the mechanism of a propagating slip pulse, including enhanced velocity weakening friction promoting self-healing of propagating ruptures (Heaton, 1990; Rice, 2006), the generation of healing phases by heterogeneous stress and strength (Beroza & Mikumo, 1996; Oglesby & Day, 2002) or by the presence of a low-velocity fault zone (Huang & Ampuero, 2011; Thakur et al., 2020), or transient changes of normal stress induced by bi-material effects (Andrews & Ben-Zion, 1997). Our results indicate that a gentle rise to the main peak in the unfiltered, fault-parallel velocity observed at Station 93048 (Figure S11 in Supporting Information S1) would be inconsistent with a steeper rise expected from slip-weakening friction with much smaller D_c ($D_c \lesssim 0.1$ m) (Figure S12 in Supporting Information S1) or enhanced velocity weakening friction without off-fault plasticity. Near-fault records, such as the ones used in this study, combined with dynamic rupture simulations may help elucidating the mechanism of a propagating slip pulse during large earthquakes.

5. Conclusions

Relatively simple, dynamic rupture models reproduce the near-fault velocity waveforms and source characteristics of the Kumamoto earthquake. Large velocity pulses recorded at the near-fault stations were likely caused by pulse-like rupture propagation on the fault. Large (> a few m/s), long-period (a few seconds) ground velocities observed in the near-fault regions (within ±1 km from the fault trace) can be explained by the interaction of the propagating subshear rupture and that reflected by the Earth's surface, which is enhanced by the rupture process on a fault bisecting shallow low-velocity layers. Since our proposed mechanism for the generation of large,

long-period ground velocities is quite general, near-fault regions in any surface-breaking, strike-slip earthquake are prone to such large, long-period velocity ground motions, which are relevant for the designs of tall buildings and large infrastructures. Our study highlights that the dynamic interaction of propagating rupture with the Earth's surface, which is not currently incorporated in most kinematic ground-motion models, is an important physical characteristics for predicting near-fault ground motions.

Data Availability Statement

Numerical outputs used to produce the figures is available at https://doi.org/10.5281/zenodo.6547678. The simulation code used in this study was developed by Ampuero (2002) and Kaneko et al. (2008). The Japan Meteorological Agency (JMA) strong-motion waveform data used in this study is publicly available and can be downloaded from the JMA webpage (in Japanese only) (https://www.data.jma.go.jp/svd/eqev/data/kyoshin/jishin/1604160125_kumamoto/index2.html). The KiK-net strong-motion waveform data can be downloaded from the NIED KiK-net server webpage (https://www.kyoshin.bosai.go.jp/kyoshin/search/index_en.html, via entering the origin time of the 16 April 2016 Kumamoto earthquake; registration (free) is required).

Acknowledgments
This study was supported by JSPS KAKENHI grants (20K22368, 21H05206), and Marsden fund awarded by the Royal Society of New Zealand. The authors thank two anonymous reviewers for their comments that helped us greatly improve the manuscript. Numerical simulations were run on both the FUJITSU Supercomputer PRIMEHPC FX1000 (Wisteria/BDEC-01) in the Information Technology Center, the University of Tokyo, and the New Zealand eScience Infrastructure (NeSI) high-performance computing facilities.

References

Abrahamson, N. A., & Somerville, P. G. (1996). Effects of the hanging wall and footwall on ground motions recorded during the Northridge earthquake. *Bulletin of the Seismological Society of America*, *86*(1B), S93–S99. https://doi.org/10.1785/bssa08601b0s93

Ampuero, J.-P. (2002). *Etude physique et numrique de la nuclation des sismes*, PhD thesis, Univ. Paris 7, Denis Diderot, Paris.

Andrews, D. J., & Ben-Zion, Y. (1997). Wrinkle-like slip pulse on a fault between different materials. *Journal of Geophysical Research*, *102*, 553–571. https://doi.org/10.1029/96JB02856

Asano, K., & Iwata, T. (2016). Source rupture processes of the foreshock and mainshock in the 2016 Kumamoto earthquake sequence estimated from the kinematic waveform inversion of strong motion data. *Earth Planets and Space*, *68*(1), 147.

Barka, A. (1999). The 17 august 1999 Izmit earthquake. *Science*, *285*(5435), 1858–1859. https://doi.org/10.1126/science.285.5435.1858

Bernard, P., & Baumont, D. (2005). Shear Mach wave characterization for kinematic fault rupture models with constant supershear rupture velocity. *Geophysical Journal International*, *162*, 431–447. https://doi.org/10.1111/j.1365-246x.2005.02611.x

Beroza, G. C., & Mikumo, T. (1996). Short slip duration in dynamic rupture in the presence of heterogeneous fault properties. *Journal of Geophysical Research*, *101*(B10), 22449–22460. https://doi.org/10.1029/96jb02291

Bizzarri, A., & Cocco, M. (2005). 3D dynamic simulations of spontaneous rupture propagation governed by different constitutive laws with rake rotation allowed. *Annals of Geophysics*, *48*(2)

Boore, D. M., & Joyner, W. B. (1997). Site amplifications for generic rock sites. *Bulletin of the Seismological Society of America*, *87*(2), 327–341. https://doi.org/10.1785/bssa0870020327

Cochran, E. S., Li, Y.-G., Shearer, P. M., Barbot, S., Fialko, Y., & Vidale, J. E. (2009). Seismic and geodetic evidence for extensive, long-lived fault damage zones. *Geology*, *37*(4), 315–318. https://doi.org/10.1130/g25306a.1

Convers, J. A., & Newman, A. V. (2011). Global evaluation of large earthquake energy from 1997 through mid-2010. *Journal of Geophysical Research*, *116*(B8). https://doi.org/10.1029/2010JB007928

Dalguer, L. A., Miyake, H., Day, S. M., & Irikura, K. (2008). Surface rupturing and buried dynamic-rupture models calibrated with statistical observations of past earthquakes. *Bulletin of the Seismological Society of America*, *98*(3), 1147–1161. https://doi.org/10.1785/0120070134

Day, S. M., Dalguer, L. A., Lapusta, N., & Liu, Y. (2005). Comparison of finite difference and boundary integral solutions to three-dimensional spontaneous rupture. *Journal of Geophysical Research*, *110*, B12307. https://doi.org/10.1029/2005JB003813

Dunham, E. M., & Archuleta, R. J. (2004). Evidence for a supershear transition during the 2002 Denali fault earthquake. *Bulletin of the Seismological Society of America*, *94*(6B), 256–268. https://doi.org/10.1785/0120040616

Dunham, E. M., & Archuleta, R. J. (2005). Near-source ground motion from steady state dynamic rupture pulses. *Geophysical Research Letters*, *32*, L03302. https://doi.org/10.1029/2004GL021793

Fukahata, Y., & Hashimoto, M. (2016). Simultaneous estimation of the dip angles and slip distribution on the faults of the 2016 Kumamoto earthquake through a weak nonlinear inversion of InSAR data. *Earth Planets and Space*, *68*(1), 1–10. https://doi.org/10.1186/s40623-016-0580-4

Goto, H., & Sawada, S. (2010). Trade-offs among dynamic parameters inferred from results of dynamic source inversion. *Bulletin of the Seismological Society of America*, *100*(3), 910–922. https://doi.org/10.1785/0120080250

Goto, H., Toyomasu, A., & Sawada, S. (2019). Delayed subevents during the Mw6.2 first shock of the 2016 Kumamoto, Japan, earthquake. *Journal of Geophysical Research*, *124*, 13112–13123. https://doi.org/10.1029/2019JB018583

Hao, J., Ji, C., & Yao, Z. (2017). Slip history of the 2016 Mw 7.0 Kumamoto earthquake: Intraplate rupture in complex tectonic environment. *Geophysical Research Letters*, *44*(2), 743–750. https://doi.org/10.1002/2016gl071543

Harris, R. A., Barall, M., Aagaard, B., Ma, S., Roten, D., Olsen, K., et al. (2018). A suite of exercises for verifying dynamic earthquake rupture codes. *Seismological Research Letters*, *89*(3), 1146–1162. https://doi.org/10.1785/0220170222

Heaton, T. H. (1990). Evidence for and implications of self-healing pulses of slip in earthquake rupture. *Physics of the Earth and Planetary Interiors*, *64*, 1–20. https://doi.org/10.1016/0031-9201(90)90002-f

Hu, F., Oglesby, D. D., & Chen, X. (2019). The sustainability of free-surface-induced supershear rupture on strike-slip faults. *Geophysical Research Letters*, *46*(16), 9537–9543. https://doi.org/10.1029/2019gl084318

Huang, Y., & Ampuero, J.-P. (2011). Pulse-like ruptures induced by low-velocity fault zones. *Journal of Geophysical Research*, *116*(B12). https://doi.org/10.1029/2011jb008684

Ida, Y. (1972). Cohesive force across the tip of a longitudinal-shear crack and Griffith's specific surface energy. *Journal of Geophysical Research*, *77*, 3796–3805. https://doi.org/10.1029/JB077i020p03796

Ide, S., & Takeo, M. (1997). Determination of constitutive relations of fault slip based on seismic wave analysis. *Journal of Geophysical Research*, *102*(B12), 27379–27391. https://doi.org/10.1029/97jb02675

Irikura, K., Kurahashi, S., & Matsumoto, Y. (2019). Extension of characterized source model for long-period ground motions in near-fault area. *Pure and Applied Geophysics*, *177*(5), 2021–2047.

Irikura, K., & Miyake, H. (2011). Recipe for predicting strong ground motion from crustal earthquake scenarios. *Pure and Applied Geophysics*, *168*(1–2), 85–104. https://doi.org/10.1007/s00024-010-0150-9

IRIS DMC. (2013). *Data services products: EQEnergy earthquake energy & rupture duration*. https://doi.org/10.17611/DP/EQE.1

Ji, C., Helmberger, D. V., David, W. J., & Kuo-Fong, M. (2003). Slip history and dynamic implications of the 1999 Chi-Chi, Taiwan, earthquake. *Journal of Geophysical Research*, *108*(B9). https://doi.org/10.1029/2002jb001764

Kanamori, H., & Anderson, D. L. (1975). Theoretical basis of some empirical relations in seismology. *Bulletin of the Seismological Society of America*, *65*, 1073–1095.

Kaneko, Y., Ampuero, J.-P., & Lapusta, N. (2011). Spectral-element simulations of long-term fault slip: Effect of low-rigidity layers on earthquake-cycle dynamics. *Journal of Geophysical Research*, *116*. https://doi.org/10.1029/2011JB008395

Kaneko, Y., Fukuyama, E., & Hamling, I. J. (2017). Slip-weakening distance and energy budget inferred from near-fault ground deformation during the 2016 M_w7. 8 Kaikōura earthquake. *Geophysical Research Letters*, *44*(10), 4765–4773. https://doi.org/10.1002/2017GL073681

Kaneko, Y., & Lapusta, N. (2010). Supershear transition due to a free surface in 3-D simulations of spontaneous dynamic rupture on vertical strike-slip faults. *Tectonophysics*, *493*, 272–284. https://doi.org/10.1016/j.tecto.2010.06.015

Kaneko, Y., Lapusta, N., & Ampuero, J.-P. (2008). Spectral element modeling of spontaneous earthquake rupture on rate and state faults: Effect of velocity-strengthening friction at shallow depths. *Journal of Geophysical Research*, *113*, B09317. https://doi.org/10.1029/2007JB005553

Kaneko, Y., & Shearer, P. M. (2014). Seismic source spectra and estimated stress drop derived from cohesive-zone models of circular subshear rupture. *Geophysical Journal International*, *197*, 1002–1015. https://doi.org/10.1093/gji/ggu030

Kearse, J., & Kaneko, Y. (2020). On-fault geological fingerprint of earthquake rupture direction. *Journal of Geophysical Research: Solid Earth*, *125*(9), e2020JB019. https://doi.org/10.1029/2020jb019863

Kobayashi, H., Koketsu, K., & Miyake, H. (2017). Rupture processes of the 2016 Kumamoto earthquake sequence: Causes for extreme ground motions. *Geophysical Research Letters*, *44*(12), 6002–6010. https://doi.org/10.1002/2017gl073857

Koketsu, K., Miyake, H., & Suzuki, H. (2012). Japan integrated velocity structure model version 1. *Proceedings of the 15th World Conference on Earthquake Engineering*, 1773.

Kubo, H., Suzuki, W., Aoi, S., & Sekiguchi, H. (2016). Source rupture processes of the 2016 Kumamoto, Japan, earthquakes estimated from strong-motion waveforms. *Earth Planets and Space*, *68*(1), 1–13. https://doi.org/10.1186/s40623-016-0536-8

Ma, S., & Archuleta, R. J. (2006). Radiated seismic energy based on dynamic rupture models of faulting. *Journal of Geophysical Research*, *111*. https://doi.org/10.1029/2005JB004055

Macklin, C., Kaneko, Y., & Kearse, J. (2021). Coseismic slickenlines record the emergence of multiple rupture fronts during a surface-breaking earthquake. *Tectonophysics*, *808*, 228834. https://doi.org/10.1016/j.tecto.2021.228834

Melgar, D., & Hayes, G. P. (2017). Systematic observations of the slip pulse properties of large earthquake ruptures. *Geophysical Research Letters*, *44*(19), 9691–9698. https://doi.org/10.1002/2017gl074916

Mikumo, T., Olsen, K. B., Fukuyama, E., & Yagi, Y. (2003). Stress-breakdown time and slip-weakening distance inferred from slip-velocity functions on earthquake faults. *Bulletin of the Seismological Society of America*, *93*(1), 264–282. https://doi.org/10.1785/0120020082

Morii, T., Sugino, M., & Hayashi, Y. (2020). *The Effects of pulse-like ground motions near fault on response and damage of buildings, 17th World Conference on Earthquake Engineering*. 2c–0244.

Oglesby, D. D., & Day, S. M. (2002). Stochastic fault stress: Implications for fault dynamics and ground motion. *Bulletin of the Seismological Society of America*, *92*(8), 3006–3021. https://doi.org/10.1785/0120010249

Palmer, A. C., & Rice, J. R. (1973). The growth of slip surfaces in the progressive failure of over-consolidated clay. *Proceedings of the Royal Society of London A*, *332*, 527–548.

Pitarka, A., Dalguer, L. A., Day, S. M., Somerille, P. G., & Dan, K. (2009). Numerical study of ground-motion differences between buried-rupturing and surface-rupturing earthquakes. *Bulletin of the Seismological Society of America*, *99*, 1521–1537. https://doi.org/10.1785/0120080193

Rice, J. R. (2006). Heating and weakening of faults during earthquake slip. *Journal of Geophysical Research*, *111*. https://doi.org/10.1029/2005JB004006

Rybicki, K. R. (1992). Strike-slip faulting in the presence of low-rigidity inhomogeneities. *Bulletin of the Seismological Society of America*, *82*(5), 2170–2190.

Shirahama, Y., Yoshimi, M., Awata, Y., Maruyama, T., Azuma, T., Miyashita, Y., et al. (2016). Characteristics of the surface ruptures associated with the 2016 Kumamoto earthquake sequence, central Kyushu, Japan. *Earth Planets and Space*, *68*(1), 1–12. https://doi.org/10.1186/s40623-016-0559-1

Singh, S. K., Mena, E. A., & Castro, R. (1988). Some aspects of source characteristics of the 19 September 1985 Michoacan earthquake and ground motion amplification in and near Mexico City from strong motion data. *Bulletin of the Seismological Society of America*, *78*(2), 451–477.

Somerville, P., Irikura, K., Graves, R., Sawada, S., Wald, D., Abrahamson, N., et al. (1999). Characterizing crustal earthquake slip models for the prediction of strong ground motion. *Seismological Research Letters*, *70*(1), 59–80. https://doi.org/10.1785/gssrl.70.1.59

Thakur, P., Huang, Y., & Kaneko, Y. (2020). Effects of low-velocity fault damage zones on long-term earthquake behaviors on mature strike-slip faults. *Journal of Geophysical Research: Solid Earth*, *125*. https://doi.org/10.1029/2020JB019587

Urata, Y., Yoshida, K., Fukuyama, E., & Kubo, H. (2017). 3-D dynamic rupture simulations of the 2016 Kumamoto, Japan, earthquake. *Earth Planets and Space*, *69*(1), 150. https://doi.org/10.1186/s40623-017-0733-0

Venkataraman, A., & Kanamori, H. (2004). Observational constraints on the fracture energy of subduction zone earthquakes. *Journal of Geophysical Research*, *109*(B5). https://doi.org/10.1029/2003jb002549

Wada, K., & Goto, H. (2012). Generation mechanism of surface and buried faults: Effect of plasticity in a Shallow-Crust Structure. *Bulletin of the Seismological Society of America*, *102*(4), 1712–1728. https://doi.org/10.1785/0120110212

Weng, H., & Yang, H. (2018). Constraining frictional properties on fault by dynamic rupture simulations and near-field observations. *Journal of Geophysical Research: Solid Earth*, *123*(8), 6658–6670. https://doi.org/10.1029/2017jb015414

Yamanaka, H., Chimoto, K., Miyake, H., Tsuno, S., & Yamada, N. (2016). Observation of earthquake ground motion due to aftershocks of the 2016 Kumamoto earthquake in damaged areas. *Earth Planets and Space*, *68*(1), 1–12. https://doi.org/10.1186/s40623-016-0574-2

Ye, L., Lay, T., Kanamori, H., & Rivera, L. (2016). Rupture characteristics of major and great ($M_w \geq 7.0$) megathrust earthquakes from 1990 to 2015: 1. Source parameter scaling relationships. *Journal of Geophysical Research: Solid Earth*, *121*, 845–863. https://doi.org/10.1002/2015JB012427

Yoshimoto, K., Sato, H., & Ohtake, M. (1993). Frequency-dependent attenuation of P and S waves in the Kanto area, Japan, based on the coda-normalization method. *Geophysical Journal International*, *114*(1), 165–174. https://doi.org/10.1111/j.1365-246x.1993.tb01476.x

Yue, H., Castellanos, J. C., Yu, C., Meng, L., & Zhan, Z. (2017). Localized water reverberation phases and its impact on backprojection images. *Geophysical Research Letters*, *44*(19), 9573–9580. https://doi.org/10.1002/2017gl073254